Volume 21
Number 11
7 June 2021
Pages 2061–2296

Lab on a Chip

Devices and applications at the micro- and nanoscale

rsc.li/loc

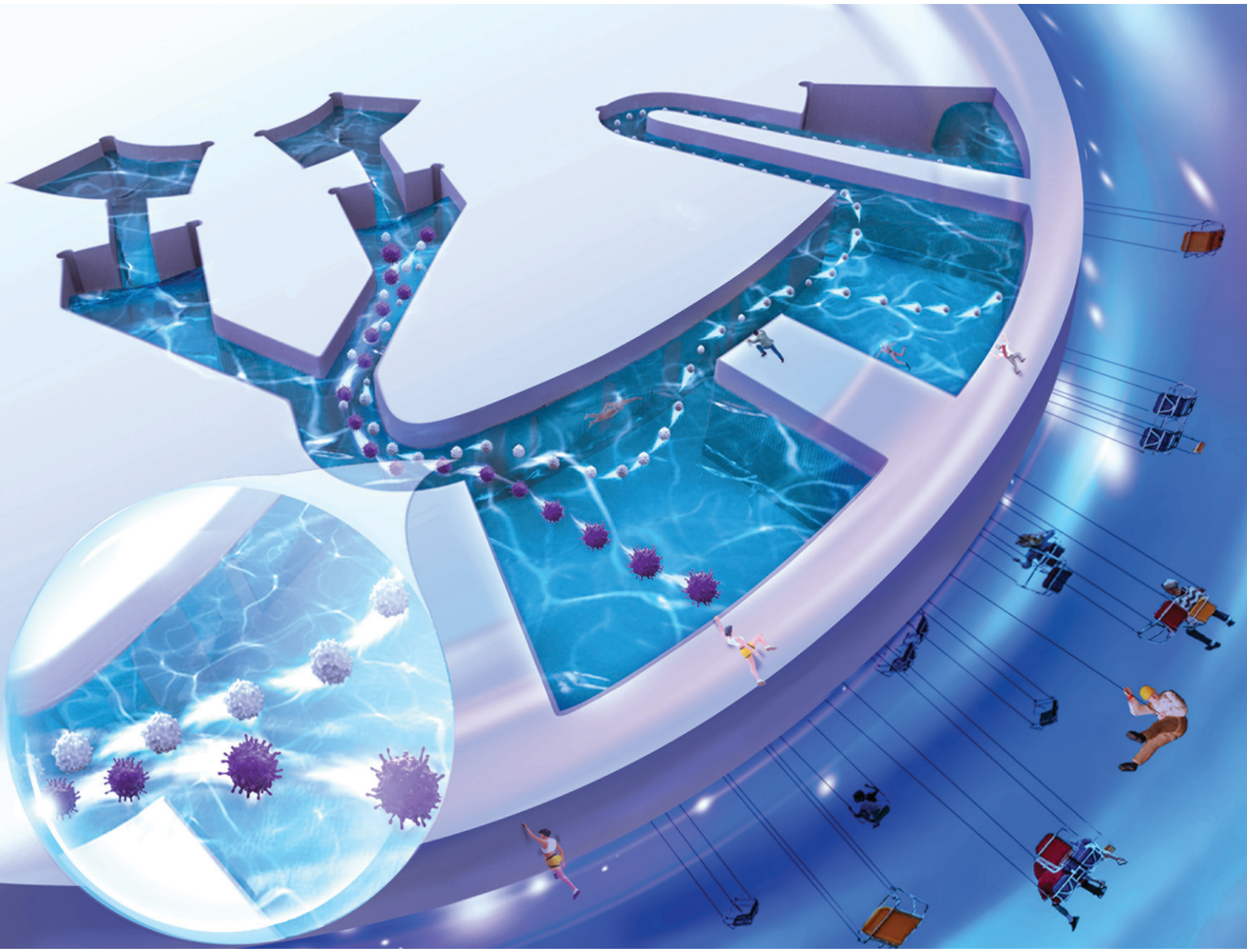

ISSN 1473-0197

ROYAL SOCIETY OF CHEMISTRY

PAPER
Junyu Ma, Yihui Wu, Yongshun Liu *et al.*
Cell-sorting centrifugal microfluidic chip with a flow rectifier

Lab on a Chip

PAPER

View Article Online
View Journal | View Issue

Cite this: *Lab Chip*, 2021, **21**, 2129

Cell-sorting centrifugal microfluidic chip with a flow rectifier†

Junyu Ma, [ab] Yihui Wu, *[a] Yongshun Liu,*[a] Yuan Ji,[ab] Mei Yang[c] and Hongquan Zhu[c]

Centrifugal microfluidic chips offer rapid, highly integrable and simultaneous multi-channel microfluidic control without relying on external pressure pumps and pipelines. Current centrifugal microfluidic chips mainly separate particles of differing density based on the sedimentation method. However, in some biological cells, the volume difference is more notable than the density difference. In particular, cancer cells are generally larger than normal cells. The instability of particle velocity caused by the non-steady flow of the fluid in the centrifugal microfluidic chip leads to low separation purity of particles of different sizes. Thus, we propose herein a centrifugal microfluidic chip with a flow rectifier that transforms the centrifugal non-steady flow into locally steady flow with continuous flow. This chip resolves the problems caused by particle sedimentation in the sample chamber and non-steady flow and greatly improves the recovery ratio and separation purity of target particles. Therefore, it can be used to separate particles of differing size. The experimental results show that the chip can separate an equal-volume mixture of 25 μm and 12 μm polystyrene particles diluted 50 times with a ratio of 1 : 6 and obtain a recovery ratio and separation purity better than 95% for the 25 μm particles. In addition, rare tumour cells are separated from high-concentration white blood cells (ratio 1 : 25) with a recovery ratio of 90.4% ± 2.4% and separation purity of 83.0% ± 3.8%. In conclusion, this chip is promising for sorting of various biological cells and has significant potential for use in biomedical and clinical applications.

Received 17th March 2021,
Accepted 14th April 2021

DOI: 10.1039/d1lc00217a

rsc.li/loc

1 Introduction

The separation of specific cells in body samples is the basis of many biomedical analytical techniques. Specifically, such techniques often require precise separation of target cells or particles from samples.[1] To date, much research has focused on pressure-driven microfluidic chips. However, the use of pressure pumps makes it difficult to integrate the whole system. The centrifugal microfluidic chip overcomes this limitation and can realise simultaneous and rapid multi-channel microfluidic control. In contrast with pressure-driven methods, the centrifugal microfluidic chip offers the advantage of facile system integration.[2]

In centrifugal microfluidic sorting methods, the density and volume of particles allow different particles to be separated. Given that centrifugal sedimentation is more sensitive to differences in density, particles of different densities are easier to separate by centrifugation.[3] Therefore, these methods are mainly applied to blood separation and to the separation of particles that differ in density.[4–9] However, for some particles, the volume difference is more notable than the density difference.[10–13] For example, cancer cells are generally larger than normal cells;[14,15] even tumour cells of small-cell lung cancer are larger than circulating lymphocytes.[16] Therefore, particle sorting methods must be developed based on volume differences. Unfortunately, on the micron scale, the complex coupling between the centrifugal field and the flow field makes it difficult to separate particles based on volume differences.

Morijiri *et al.*[17] compared the experimental results of separating 5 μm from 3 μm polystyrene particles with the same sorting structure by pressure-driven and centrifugal-driven methods. Their results show that, at a low flow rate and under a steady pressure-driven flow, the different particles emerge from different outlets with good separation. However, under centrifugal non-steady flow, the different particles flow from multiple outlets and are mixed, resulting

[a] *State Key Laboratory of Applied Optics, Changchun Institute of Optics, Fine Mechanics and Physics (CIOMP), Chinese Academy of Sciences, Changchun, China. E-mail: yihuiwu@ciomp.ac.cn, liuyongshun1981@163.com; Fax: +86 0431 85690271; Tel: +86 0431 86176135*
[b] *School of optoelectronics, University of Chinese Academy of Sciences, Beijing, China*
[c] *Department of Clinical Laboratory, The Second Hospital of Jilin University, Changchun, China*

† Electronic supplementary information (ESI) available. See DOI: 10.1039/d1lc00217a

in a poor separation. Thus, the varying flow rate in the centrifugal non-steady flow makes it difficult to accurately control the particle trajectory.

Yeo *et al.*[18] used passive pressure-driven centrifugal fluid flow coupled with centrifugal force acting on particles within microfluidic chips to separate 20 μm from 10 μm polystyrene particles, but the separation efficiency was only 70%. A greater separation efficiency was observed for greater differences in particle diameter. For example, a separation efficiency of 90% is achieved for separating 20 μm from 2 μm particles. Moreover, some particles remain in the separation channel because, as the centrifugal non-steady flow ceases, the fluid also stops flowing. Under the action of centrifugal force, the particles sedimentate at the bottom of the channel instead of flowing into the collection chamber, which reduces the separation efficiency. This phenomenon significantly impacts detection experiments, such as separating and counting rare cells, which require high separation efficiency.

To summarise, microscale particles have a high surface-to-volume ratio. Smaller particles in the fluid experience a smaller volume force in the centrifugal field relative to the surface force in the flow field. The centrifugal non-steady flow leads to rapid changes in particle velocity, which makes the particle trajectory less controllable and affects the separation purity. To address these problems, we propose herein a cell-sorting centrifugal microfluidic chip with a flow rectifier, which transforms the centrifugal non-steady flow into locally steady flow with continuous flow.

To begin, we designed a simulation to compare the flow rates at the outlet of the sample chamber with and without the flow rectifier. Theoretically, this reveals the effect of the flow rectifier. We also simulate the particle trajectories under a steady flow field as a function of the rotation speed of the centrifugal microfluidic chip. The simulation results indicate that particles with the same density but different diameters are separated in both the centrifugal field and the flow field, which is indicative of the sorting ability of the chip.

Next, to experimentally verify the sorting ability of the centrifugal microfluidic chip, we experimentally sorted particles and cells. First, a comparative experiment was set up by alternating the use of the flow rectifier to analyse how it affects particle sorting in centrifugal non-steady flow. The experimental results show that, with the flow rectifier, the centrifugal non-steady flow tends toward steady flow, and the separation purity increases by 63.2%. Second, the experimental results with different rotation speeds are similar to the results of the simulation. The particles are introduced into the separation chamber due to the action of the steady flow field. The mixed 25 and 12 μm polystyrene particles of equal density are separated by nearly 100% without residues, with a separation purity exceeding 95%.

In addition, we carried out sorting experiments on the mixture of 25 and 12 μm particles of varying concentrations and ratios to further characterise the sorting performance of the centrifugal microfluidic chip. The results show that the separation purity increases to nearly 100% with decreasing concentration and ratio of the two kinds of particles. To further analyse the sorting performance of these chips, we experimentally separated mixtures of 15 μm and 8 μm particles. With the chip depth at 70 μm, the recovery ratio and separation purity are 95.2% ± 3.4% and 80.0% ± 2.6%, respectively.

Furthermore, to verify the practicability of the proposed method, we experimentally separated prostate cancer cells from high-concentration white blood cells (WBCs). The recovery ratio for prostate cancer cells is 90.4% ± 2.4%, and the separation purity is 80.3% ± 3.8%.

The results of these sorting experiments involving particles and cells indicate that the centrifugal microfluidic chip is promising for sorting of various biological cells. It is therefore expected to play a significant role in biomedical and clinical applications.

2 Theory and mechanism

2.1 Principle of cell sorting

As shown in Fig. 1, the fluid in the centrifugal microfluidic chip is subjected to a centrifugal force, Coriolis force, and Euler force,[19] which are given by

$$\vec{F}_{\mathrm{Cen}} = -\rho\vec{\omega} \times (\vec{\omega} \times \vec{r}) \quad (1)$$

$$\vec{F}_{\mathrm{Cor}} = -2\rho\vec{\omega} \times \vec{u} \quad (2)$$

$$\vec{F}_{\mathrm{Eul}} = -\rho\dot{\vec{\omega}} \times \vec{r} \quad (3)$$

where ρ is the fluid density, $\vec{\omega}$ is the angular-velocity vector, $\vec{r}$ is the radial-position vector, and $\vec{u}$ is the fluidic velocity vector. The centrifugal force is always directed radially outward, the Coriolis force is typically perpendicular to both the linear-and angular-velocity vectors, and the Euler force depends on the direction of the angular acceleration. The device rotates at a constant angular velocity in this work, so $\vec{F}_{\mathrm{Eul}} = 0$ in eqn (3).

Fig. 2 shows the principle behind sorting tumour cells from WBCs with a centrifugal microfluidic chip with a flow

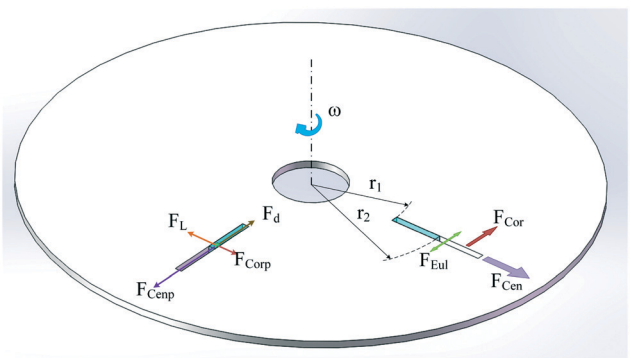

Fig. 1 Schematic diagram showing the forces on the fluid and particles in a centrifugal microfluidic device rotating at a constant angular velocity.

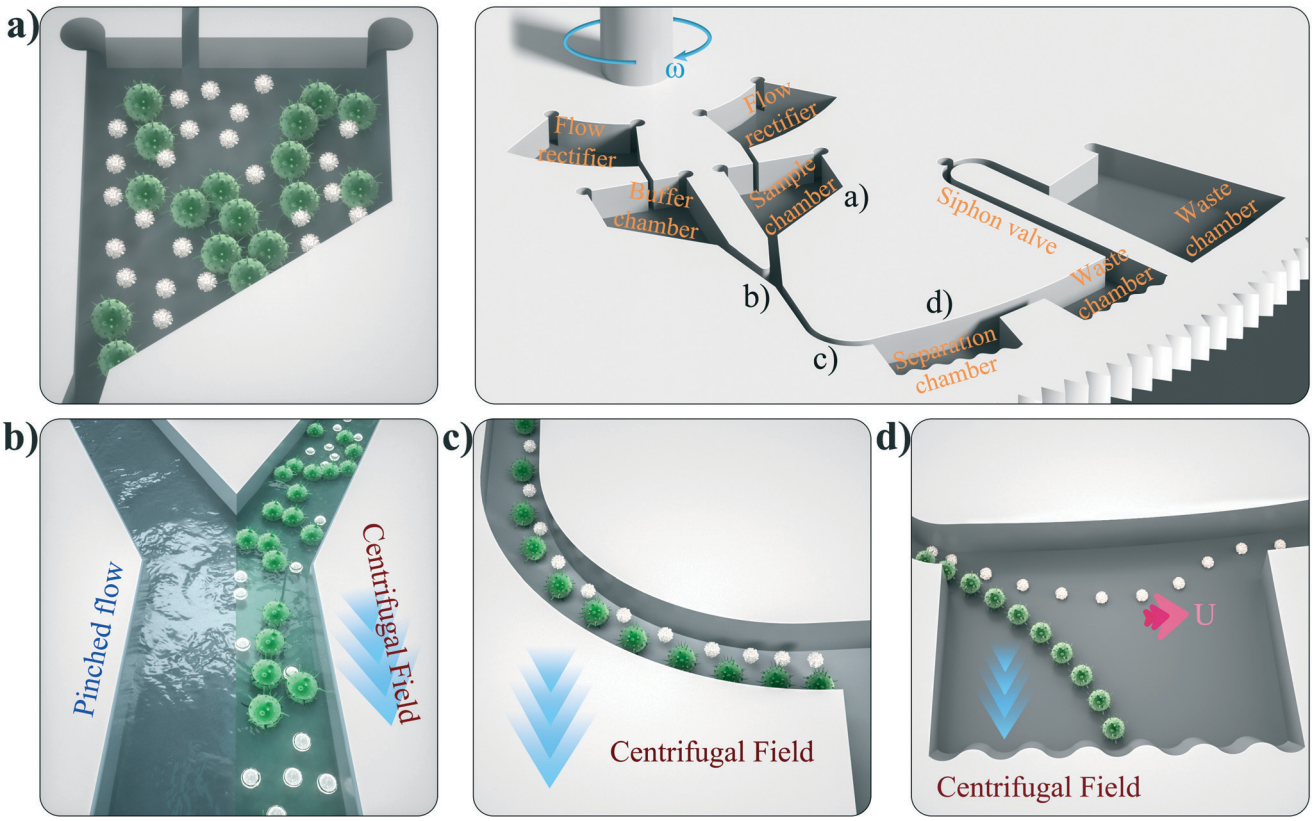

Fig. 2 Schematic illustrations showing the sorting mechanism of the centrifugal microfluidic chip with a flow rectifier. Panels a)–d) show enlarged views of areas a)–d), respectively. Panel a) shows the tumour cell and WBC mixture in the sample chamber. Due to the pinched flow, the cells suspended in the liquid move along the right side of the channel, as shown in panel b). Panel c) shows how, in the bend, the direction of cell movement deviates from the direction of the centrifugal force. The tumour cell and WBC trajectories vary due to the different net forces, resulting in initial separation of tumour cells from WBCs. Panel d) shows how cells are separated in the separation chamber due to different net forces. Tumour cells sedimentate in the separation chamber, whereas WBCs flow out.

rectifier. The chip consists of a flow rectifier, a sample chamber, a buffer chamber, a pinched flow channel, a separation chamber, a siphon valve with a vent,[20] and two waste chambers. The cell suspension is introduced into the sample chamber as shown in Fig. 2a. The flow rectifier causes the fluid to tend toward a local steady flow under the centrifugal force.

Next, in the pinched flow[21] shown in Fig. 2b, the cells suspended in the liquid move along the right side of the channel. In this process, the cells are under the combined action of centrifugal force, Coriolis force, inertial lift force, and flow resistance. Fig. 2c shows that, once the cells reach the bend, the direction of cell movement deviates from the direction of the centrifugal force. The tumour cell and WBC trajectories thus change due to the influence of the different forces, producing an initial separation. Next, the cells enter the separation chamber (Fig. 2d). The significant widening of the structure leads to a substantial decrease in flow rate that further increases the difference in net force on tumour cells *versus* WBCs in the separation chamber, resulting in different trajectories for the two cell types. At this point, the flow rate in the separation chamber is constant. Because of the different resultant forces, tumour cells sedimentate in the separation chamber, and WBCs flow out with the fluid, thereby sorting tumour cells from WBCs.

2.2 Theoretical analysis

To determine the flow field, this study uses a laminar incompressible flow model with no-slip boundary conditions. Based on the Navier–Stokes equation for incompressible fluids, the equations used to simulate the mass and momentum transfer of fluid are

$$\rho\frac{\partial\vec{u}}{\partial t}+\rho(\vec{u}\cdot\nabla)\vec{u}=\nabla\cdot\left[-p\vec{I}+\mu\left(\nabla\vec{u}+(\nabla\vec{u})^{T}\right)\right]+\vec{f}$$
$$\nabla\cdot\vec{u}=0 \quad (4)$$

where μ is the dynamic viscosity of the fluid, p is the pressure, $\vec{I}$ is the unitary tensor, and $\vec{f}$, which is the sum of $\vec{F}_{\mathrm{Cen}}$ and $\vec{F}_{\mathrm{Cor}}$ in the centrifugal chip, is the volume force acting on the fluid. Newton's second law of motion is used to predict the trajectory of particles:

$$\frac{\mathrm{d}(m_{\mathrm{p}}\vec{v}_{\mathrm{p}})}{\mathrm{d}t}=\vec{F}_{\mathrm{Cenp}}+\vec{F}_{\mathrm{Corp}}+\vec{F}_{\mathrm{L}}+\vec{F}_{\mathrm{d}} \quad (5)$$

where m_p and $\vec{v}_p$ are the particle mass and velocity vector, respectively, and $\vec{F}_{Cenp}$, $\vec{F}_{Corp}$, $\vec{F}_L$, and $\vec{F}_d$ are the centrifugal, Coriolis, lift and Stokes' drag forces on the particles, respectively (see the ESI† for details).

2.3 Numerical methods

The governing equations were solved using the finite-element method. To simulate the change of flow rate at the sample-chamber inlet, we used the level-set method to describe the fluid interface. Considering the influence of surface tension, the Navier–Stokes equation takes the form

$$\rho\frac{\partial\vec{u}}{\partial t}+\rho(\vec{u}\cdot\nabla)\vec{u}=\nabla\cdot\left[-p\vec{I}+\mu\left(\nabla\vec{u}+(\nabla\vec{u})^T\right)\right]+\vec{f}_{st}+\vec{f}$$
$$\nabla\cdot\vec{u}=0 \quad (6)$$

where $\vec{f}_{st}$ is the surface tension at the air–water interface. In the level set interface, the surface tension is

$$\vec{f}_{st}=\sigma\delta\kappa\vec{n} \quad (7)$$

where σ is the surface tension coefficient, δ is the Dirac delta function and is nonzero only at the fluid interface, $\kappa=-\nabla\cdot\vec{n}$ is the curvature and $\vec{n}$ is the normal to the interface. To determine the velocity and concentration fields, we solved the Navier–Stokes equations for fluid flow and the convection–diffusion equation. For the fluid inlets, outlets and air vents of the fluid domain, we used open boundary conditions, whereas no-slip boundary conditions are applied to all other boundaries.

To simulate particle trajectories, Newton's second law of motion was solved by the Lagrangian approach. Because the flow rectifier in the chip used herein promotes steady flow, we used the laminar steady incompressible flow model with no-slip boundary conditions on the channel walls to determine the flow field. Pinched flow makes particles flow in from the right of the channel inlet, and we assumed a random particle distribution. The walls have no-slip boundary conditions, the outlets are assigned zero-gauge pressure, and the flow rate is fully developed at the inlet. The inlet flow is determined by eqn (S9).†

3 Materials and methods

3.1 Design and fabrication of the microfluidic chip

For centrifugal non-steady flow in the separation chamber, Fig. 3a shows the trajectories of two particles of differing diameter. The decrease of flow rate moves forward the sedimentation position of particles, and the two types of particles mix together, which reduces the separation purity. To improve the separation purity, the flow rectifier (see Fig. 2) is designed to transform the non-steady flow into a steady flow. Under steady flow, when different-size particles flow in from a given position at the separation-chamber inlet, they sedimentate at different positions, as shown in Fig. 3b, which sorts particles of differing diameters. However, in practice, particles may flow in from arbitrary positions at the inlet of the separation chamber, as shown in Fig. 3c. Thus, even particles that differ significantly in diameter are difficult to separate. The ideal situation is for large particles to flow in from below the inlet of the separation chamber, and for small particles to flow in from the top of the inlet of the separation chamber, which leads to optimal sorting for this chip. Toward this end, we designed a pinched flow structure to force particles to move to the right side of the channel (see Fig. 2b) so that different-size particles are initially separated in the bend channel (see Fig. 2c). This separation is further enlarged in the separation chamber, leading to the separation of particles of different sizes.

The microfluidic chip was fabricated by using soft lithography. The microstructures were fabricated on a silicon chip by using a micro-nano process and inverted twice with liquid polydimethylsiloxane (PDMS) to get a PDMS structure. The final PDMS structure was fabricated with holes and cavities punched after moulding. The glass and PDMS structures were bonded after exposure to oxygen plasma, and the chip chamber was sealed with single-sided adhesive after bonding. The final product was a complete centrifugal microfluidic chip.

3.2 Sample preparation

To test the performance of the chip, we experimented with two types of fluorescent polystyrene particles with diameters of approximately 25, 12, 15, and 8 μm (Tianjin Baseline Chromtech Research Centre, Tianjin, China). The particle-solution concentrations obtained from the blood counting

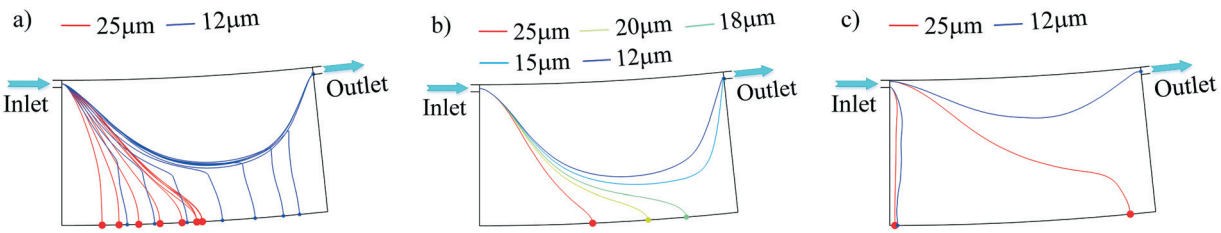

Fig. 3 Simulated trajectories of different-size particles in the separation chamber. Panel a) shows trajectories of two different-size particles in the centrifugal non-steady flow. Panel b) shows trajectories of different-size particles that enter the separation chamber from the same position in the steady flow. Panel c) illustrates how particles flow in from arbitrary positions at the entrance of the separation chamber.

chamber were about 2.7×10^6, 1.71×10^7, 1.47×10^7, and 3.0×10^7 mL^{-1}. The particle solutions were then diluted with 0.5 wt% Tween 20 mixed deionised water for preparing the particle suspensions with specific concentrations and ratios. Before conducting the experiments, the particle suspensions were mixed in a blender for 30 s to obtain a substantially monodispersed suspension.

For cell experiments, human prostate cancer cells (LNCaP Clone FGC) were cultured at the Roswell Park Memorial Institute in medium (RPMI Medium 1640, Gibco) supplemented with 10% foetal bovine serum (FBS, KY), 1% penicillin–streptomycin mixture (Solarbio) and 1% sodium pyruvate (Gibco). After growing to confluence, the LNCaP cells were dissociated by using trypsin solution (0.25%, Hyclone) and then re-dispersed in the complete medium. By counting with an improved Neubauer counting plate (China), we prepared cell suspensions of the desired concentrations. The LNCaP cells were then stained with phycoerythrin (PE) anti-human prostate-specific membrane antigen (FOLH1) (BioLegend) according to the manufacturer's protocol.

The blood samples were drawn from a healthy volunteer using a vacutainer collection tube containing anticoagulant EDTA-K2. All experiments were performed in compliance with relevant guidelines and regulations for use of blood samples by the State Council of the People's Republic of China. The experimental protocols were approved by the institutional committee of Institutional Ethical Committee (IEC) for Clinical Research of the Second Hospital of Jilin University and the written informed consents were obtained from the blood donors. The whole blood was lysed with red blood cell lysis buffer (Solarbio), and the WBCs obtained were diluted with phosphate buffered saline (Hyclone) to different concentrations. The stained tumour cells and a certain concentration of the WBC suspension were centrifuged, following which the supernatant was removed, and the tumour-cell and WBC suspensions were re-suspended in bovine serum albumin buffer (Solarbio) before finally being mixed together to obtain the tumour sample model.

3.3 Experimental setup and device operation

Before running the sorting experiment, the chip injected with buffer was placed on a centrifuge and rotated to fill the chip microchannel with liquid to create a continuous-fluid environment. At this point, the liquid levels in the buffer chamber and sample chamber are balanced over the centrifugal radius at the vent of the siphon valve. After the sample is injected into the sample chamber and the buffer is injected into the buffer chamber and the flow rectifier, the sorting experiment is run. At this point, the siphon-valve vent is sealed with single-sided adhesive to force the sample to flow into the separation chamber. After the experiments, the chip was placed on an inverted fluorescence microscope (Nikon Ti2-U) to determine the sorting results of the particles or cells *via* both bright-field and fluorescence observation. The images captured were then processed with NIS-D software to create the composite images displaying the sorting performance for the particles or cells.

4 Results and discussion

4.1 Numerical simulation of the flow rate at the sample-chamber outlet

Non-steady flow is defined as the flow with a changing fluid velocity over time. In the centrifugal process, non-steady flow can affect the particle trajectory, so the flow rectifier was designed to avoid the negative effects of non-steady flow. To prove that the flow rectifier functions, we simulated the sample-chamber outlet flow rate with and without the flow rectifier (Fig. 4). Without the flow rectifier (Fig. 4a-1), the liquid level in the sample chamber decreases gradually, as does the outlet flow rate (Fig. 4a-2). Fig. 4a-3 shows the average outlet flow rate (after normalisation) at multiple times. We conclude from these results that the outlet flow rate decreases with time in centrifugal non-steady flow. With the flow rectifier, the liquid level in the flow rectifier reduces gradually over time (see Fig. 4b-1), whereas the liquid level in the sample chamber remains unchanged because more liquid flows in than that flows out.

Fig. 4b-2 shows the outlet flow rate at the corresponding time, which reveals that the flow rates at different times remain quite similar. Fig. 4b-3 shows the mean outlet flow rate at multiple times after normalisation. When using the flow rectifier, the outlet flow rate remains constant over time because pressure from the flow rectifier is released by the two vents at the upper part of the sample chamber, resulting in a stable pressure difference in the sample chamber. In addition, to maintain steady flow for a long time, the volume of the flow rectifier must significantly exceed that of the sample chamber. To satisfy this criterion, the depth of the flow rectifier was 3 mm, which is 30 times the 100 μm depth of the sample chamber. Steady flow is maintained sufficiently long for the cells to be introduced into the separation chamber and separated.

4.2 Numerical simulation of the particle trajectory in the pinched flow channel and separation chamber

To understand the sorting mechanism of the centrifugal microfluidic cell-sorting chip with steady flow, we simulated the trajectories of 25 and 12 μm equal-density polystyrene particles in the pinched flow channel and in the separation chamber in a steady flow (see Fig. S4†). Large particles sedimentate in the separation chamber and small particles flow out, which is consistent with the theoretical analysis. To determine how the rotation speed affects the particle trajectories, we repeated the simulation for rotation speeds of 2000, 2500, 3000, 3500 and 4000 rpm (see results in Fig. 5a).

When the rotation speed is less than 3500 rpm, the 25 μm particles sedimentate in the separation chamber, whereas the 12 μm particles flow out with the fluid. However, when the rotation speed reaches 4000 rpm, some small particles also

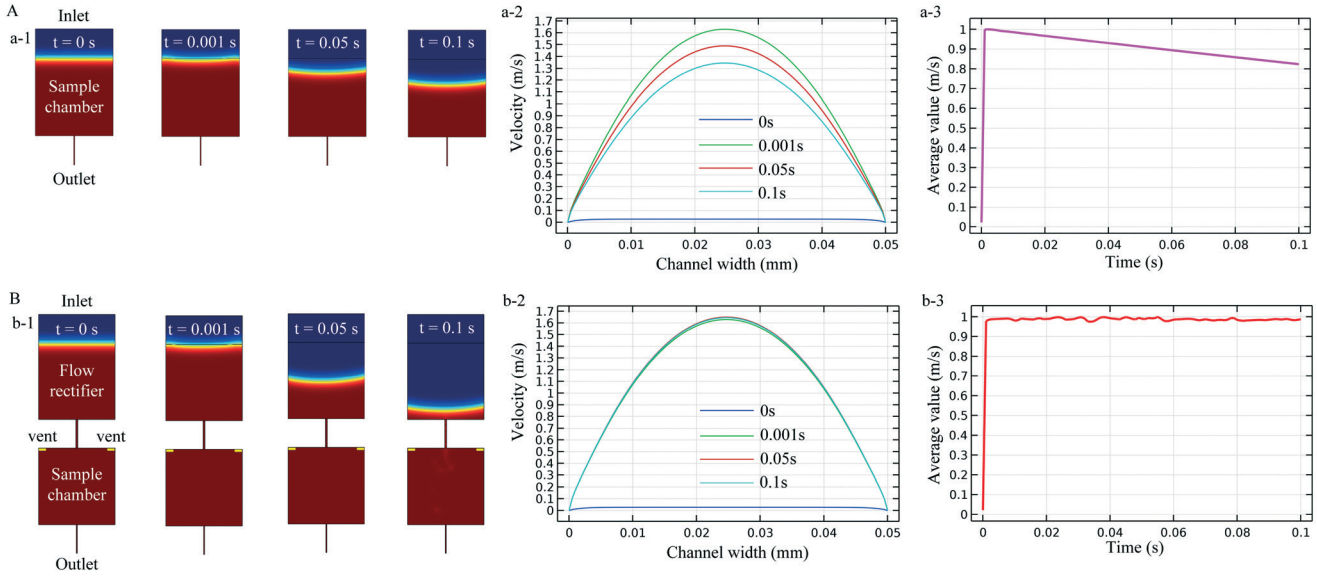

Fig. 4 Rows A and B show the simulation results of two-phase flow within 0.1 s without and with the flow rectifier, respectively. Panels a-1 and b-1 indicate the liquid level at 0, 0.001, 0.05, and 0.1 s, respectively. The outlet flow rate from the sample chamber at the same times as in panels a-1 and b-1 is shown in panels a-2 and b-2, respectively. Panels a-3 and b-3 illustrate the average outlet flow rate at multiple times after normalisation.

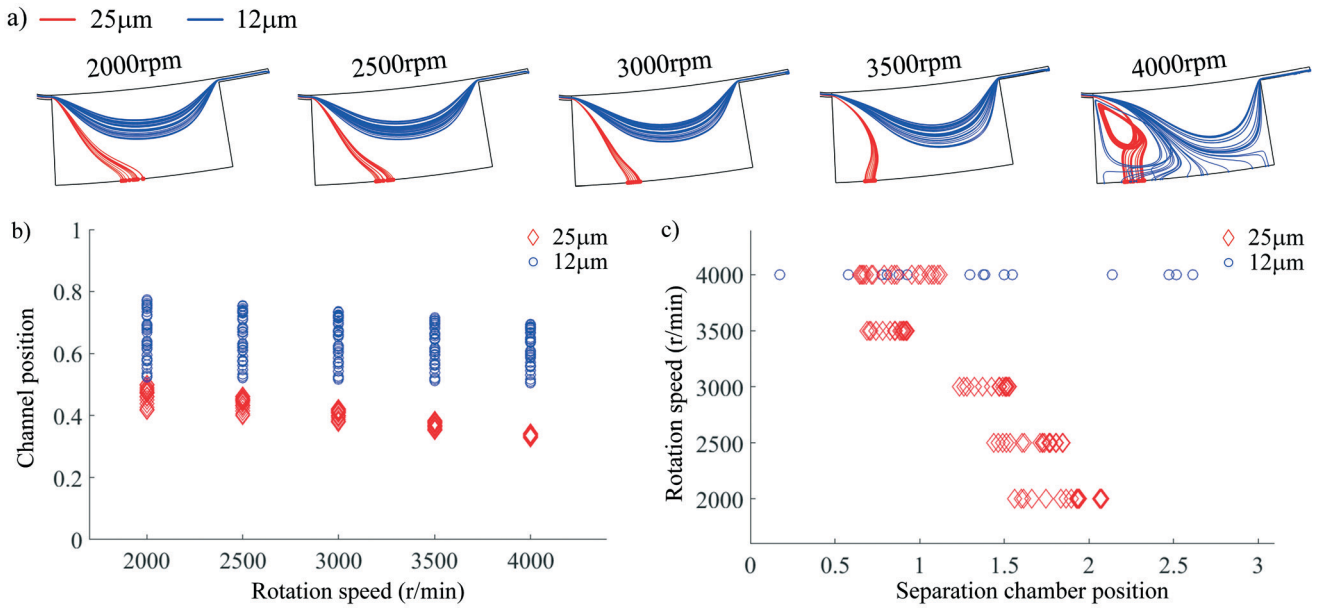

Fig. 5 Panel a) shows the numerical simulation of particle trajectories at different rotation speeds. Panel b) shows the particle distributions at the inlet of the separation chamber at different rotation speeds. Panel c) shows the different sedimentation positions of particles in the separation chamber at different rotation speeds.

sedimentate in the separation chamber because a large vortex appears in the separation chamber and affects the trajectories of the small particles. The vortex is created when a microchannel suddenly widens, which leads to fluid jetting and detachment of the boundary layer at sufficiently high Reynolds number in the channel.[22] Vortex formation depends on the fluid inertia: increasing the Reynolds number for the flow leads to an increased vortex size. Here, the Reynolds number is defined as $Re = \rho U_{max} H/\mu$ (see the ESI† for details). In Fig. S6,† the vortex appears in the separation chamber when Re = 14, but the trajectories of the small particles are not affected due to the small size of the vortex. In contrast, the larger vortex generated with Re = 18 affects the trajectories of the small particles. Therefore, some of the small particles sedimentate in the separation chamber, resulting in reduced separation purity.

To accurately characterise how particle trajectories depend on the rotation speed, Fig. 5b shows the coordinates of the particle distribution at the inlet of the separation chamber. As the rotation speed increases, the large particles gradually

take a lower position and the focusing phenomenon becomes more evident. The small particles, meanwhile, change little. This result is explained by particle migration that is mainly affected by centrifugal force, which is proportional to the rotation speed and particle diameter. As a result, varying the rotation speed changes the initial separation of particles.

Fig. 5c shows the position of particle sedimentation in the separation chamber. Combining this figure with Fig. 5b shows that the vertical dispersion of large particles at the separation-chamber inlet leads to a horizontal dispersion of the sedimentation position in the separation chamber. In other words, the higher the large particles are at the inlet, the more the sedimentation positions move backward in the separation chamber.

The vertical dispersion of particles is caused by varying the rotation speed. With a greater rotation speed, the initial separation between the large and small particles is obvious, and the large particles take a lower position, which clearly reveals the focusing phenomenon. Therefore, the sedimentation position moves forward (*i.e.*, decreases in Fig. 5c) and narrows. In particular, when the rotation speed reaches 3500 rpm, the particle positions suddenly decreases because the vortex in the separation chamber affects the trajectory of large particles. These results lead to the conclusion that the chip accurately controls the sedimentation position of particles and thereby sorts particles by size when the rotation speed is less than 3500 rpm.

4.3 Improving the particle recovery ratio and separation purity by using the flow rectifier

We compare the experimental results with and without the flow rectifier for an equal-volume mixture of 25 and 12 μm polystyrene fluorescent particles diluted 50 times. The sorting performance of the chip is characterised by its recovery ratio and separation purity. The recovery ratio is defined as the ratio of the number of target particles captured to the total number of target particles input into the chip, expressed as a percent. Separation purity is defined as the ratio of target particles captured to the total number of captured particles, expressed as a percentage. Specifically, we express the recovery ratio and separation purity as

$$\text{Recovery ratio} = 100\% \times \frac{\text{target particles}_{\text{captured}}}{\text{target particles}_{\text{input}}} \quad (8)$$

$$\text{Separation purity} = 100\% \times \frac{\text{target particles}_{\text{captured}}}{\text{all particles}_{\text{captured}}} \quad (9)$$

Rotating the chip without the flow rectifier at 2500 rpm for 60 s causes a small number of particles to sedimentate on the side wall of the sample chamber, as shown in Fig. 6a-1. This occurs because the fluid stops when the centrifugation stops. The particles sedimentate on the side wall of the sample chamber due to the centrifugal force and cannot flow

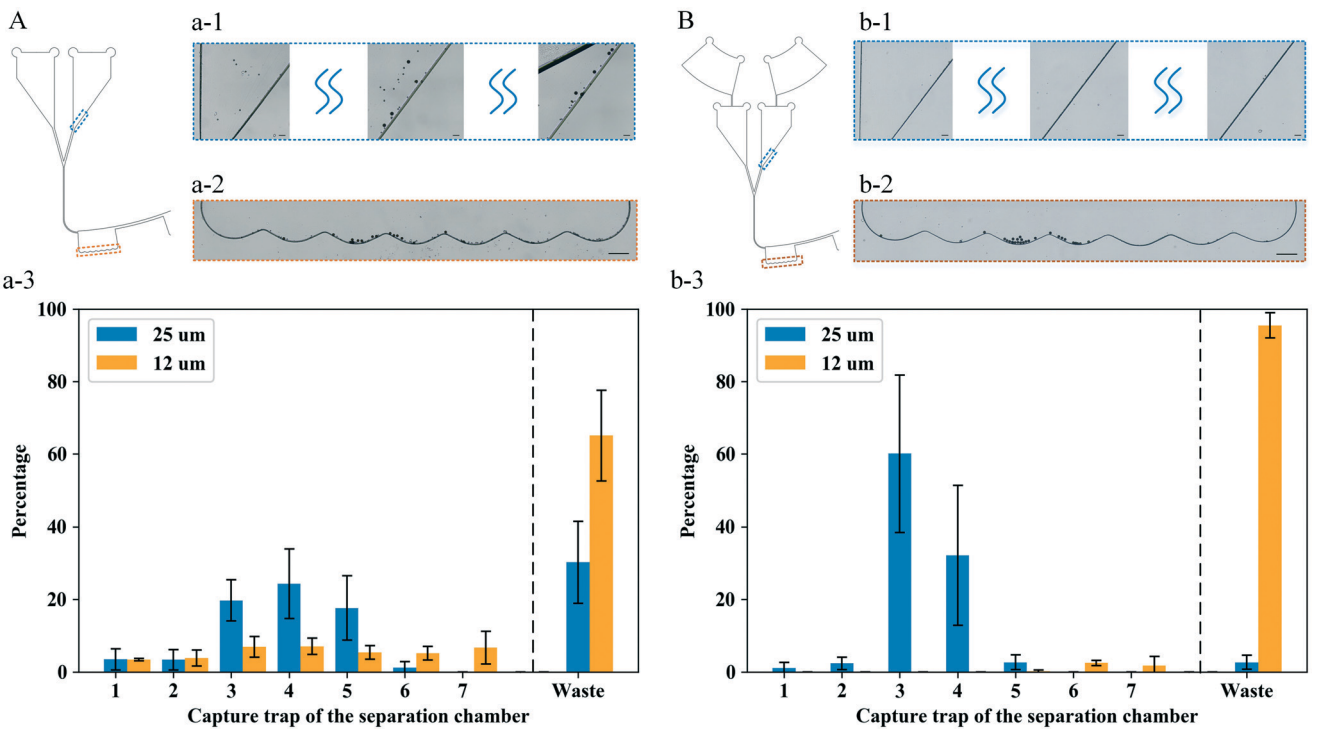

Fig. 6 Columns A and B show results without and with the flow rectifier, respectively. Panels a-1 and b-1 (scale bars: 50 μm) and a-2 and b-2 (scale bars: 50 μm) show enlarged images of particle deposition at the sidewall of the sample chamber and particle sedimentation in the separation chamber, respectively. Panels a-3 and b-3 show the fraction of particles captured as a function of the position in the separation chamber without and with the flow rectifier (n = 3).

into the separation chamber, which reduces the recovery ratio for the particles.

Fig. 6a-2 shows the particle sedimentation in the separation chamber. The large and small particles are mixed together. To accurately characterise the particle sedimentation position, Fig. 6a-3 compares the particle distribution in each capture trap with that in the waste chamber. Particles with a diameter of 25 μm sedimentate in the capture trap at positions 1–5, and some 12 μm particles sedimentate in the capture trap at positions 1–7. This occurs because the particle velocity decreases gradually, whereas the sedimentation velocity remains constant in non-steady flow. The increase in particle sedimentation position widens the range of sedimentation positions of the particles. In addition, smaller particles are more strongly influenced by the flow rate, so the separation purity of the particles decreases. In the end, the particle recovery ratio is 69.8% ± 11.3% and the separation purity is 35.6% ± 10.9%.

To address these two problems of particle retention and low purity, the flow-rectifier was designed as shown in Fig. 6B. The flow rectifier is connected at the top of both the sample chamber and buffer chamber to promote a local steady flow state and thereby reduce the effects of flow-rate variations on the particle-sedimentation position. Under the continuous flow of fluid in the sample chamber, particles deposited on the wall are also introduced in the separation chamber. The chip was also tested at 2500 rpm rotation speed for 60 s. Fig. 6b-1 shows that no target particles sedimentated on the side wall of the sample chamber, indicating that the target particles are all introduced into the separation chamber. The recovery ratio is 97.3% ± 1.9%, which was 27.5% greater than that without the flow rectifier. Fig. 6b-2 shows the obvious separation between 25 and 12 μm particles in the separation chamber, which shows the effectiveness of the flow rectifier. Fig. 6b-3 shows that most of the 25 μm particles sedimentate in capture traps 3 and 4, and a small part of the 12 μm particles sedimentate in traps 6 and 7. Most of the 12 μm particles flow out of the separation chamber. Compared with the structure without the flow rectifier, most of the 25 μm particles sedimentate at a concentrated position, and the sedimentation width of small particles reduces the distance of 5 capture traps. We conclude that the flow rectifier alleviates the difficulty caused by the centrifugal non-steady flow. The separation purity is 98.8% ± 1.7%, which is 63.2% greater than that without the flow rectifier.

4.4 Effects of the rotation speed on particle sorting

The experiments illustrate how the rotation speed affects the sedimentation positions of the particles. A suspension of 25 and 12 μm particles, mixed in equal volume and then diluted 50 times, was introduced into the sample chamber and the chip was rotated for 60 s at rotation speeds of 2000, 2500, 3000, 3500, and 4000 rpm. The results are shown in Fig. 7. Below 3500 rpm, the different-size particles are apparently separated with high separation purity, which shows that the sorting does not depend on the rotation speed. The sedimentation position of 25 μm particles moves forward with increasing rotation speed. When the rotation speed reaches 4000 rpm, the vortex causes the 12 μm particles to mix with the 25 μm particles. These experimental results are consistent with the simulation results.

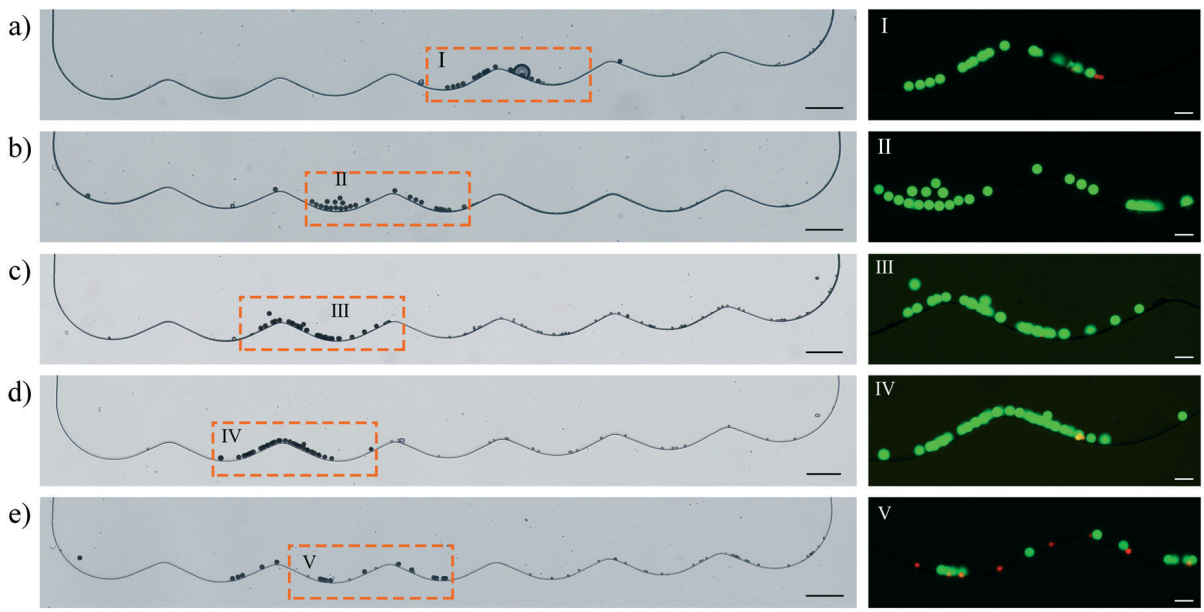

Fig. 7 The panels on the left show the 25 and 12 μm particles in the bright field (scale bar is 200 μm), and the right panels show the composite of the green and red fluorescence in the dark field with 25 (12) μm particles in green (red) (scale bars: 50 μm). Panels a)–e) show the results for the chip rotated for 60 s at 2000, 2500, 3000, 3500, and 4000 rpm, respectively.

The results indicate that the number of recycled 25 μm particles decreases at 2000 rpm. An analysis of the experimental results indicates that, at a low rotation speed, the particles flow out from the right vent of the sample chamber, which offers small resistance owing to the insufficient centrifugal force. As a result, some particles are lost, which reduces the recovery ratio.

At 4000 rpm, some particles remain on the side wall of the sample chamber, possibly because the particles sedimentated under a large centrifugal force, increasing the friction between the particles and side wall. Therefore, some particles find it difficult to flow into the separation chamber from the sample chamber at a high rotation speed, causing a low recovery ratio for the target particles.

An optical microscope was used to count the 25 μm particles and the recovery ratio and separation purity of the particles were calculated at various rotation speeds (see results in Fig. 8). The results show that the recovery ratio and separation purity of 25 μm particles exceed 90% from 2500 to 3500 rpm. The chip thus offers excellent sorting performance and high robustness.

4.5 Effects of the concentration and ratio on particle sorting

Sorting experiments with particle suspensions of differing concentrations were carried out to further characterise the sorting performance of the chip. Equal volumes of 25 and 12 μm particles were mixed and diluted 12.5 times, 25 times, and 50 times. The sorting results are shown in Fig. 9a-1–a-3. At high concentration, a few small particles sedimentate in the sedimentation area of the large particles, although this phenomenon decreases with decreasing concentration. Fig. 9b shows the recovery ratio and separation purity of the large particles. The recovery ratio is not affected by the concentration, but the separation purity increases as the concentration decreases and even approaches 100% for the particle suspension diluted 50 times. This result is tentatively attributed to the interaction between particles at high concentrations affecting the particle trajectories,[23] resulting in a few small particles falling into the same capture trap as large particles and thereby reducing the separation purity.

To understand the effect of the particle ratio, samples mixed at ratios of 1 : 12, 1 : 60, and 1 : 120 were prepared by varying the number of 12 μm particles while maintaining the number of 25 μm particles at 1.4×10^4 mL^{-1}. The samples were added to the chip and rotated for 60 s at 2500 rpm. Fig. 10a-1–a-3 show the separation results, which are similar to the results for varying concentrations; namely, the recovery ratio of large particles is independent of the particle ratio as shown in Fig. 10b. However, upon increasing the particle ratio, the separation purity gradually decreases, which is tentatively attributed to interactions between particles whereby a greater number of small particles affects the particle trajectories.

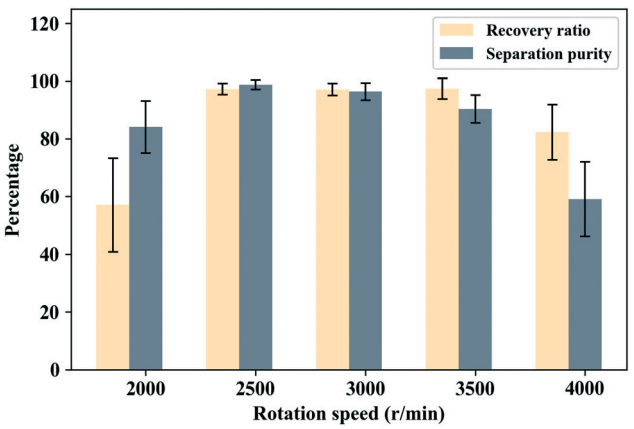

Fig. 8 Recovery ratio and separation purity of particles at rotation speeds from 2000 to 4000 rpm (n = 3).

4.6 Characterisation of separation performance for small particles

To further analyse the sorting performance of the chip, we experimented with 15 and 8 μm particle mixtures. First, the trajectories of 15 and 8 μm particles were simulated at a rotation speed of 3500 rpm. Fig. 11a shows that only a small fraction of the 15 μm particles sedimentate in the separation chamber, whereas most of the 15 μm particles and all of the 8 μm particles flow out. Second, solutions of 15 and 8 μm particles diluted 500 times and 5 times, respectively, were mixed in equal volumes and added to the chip, which was then rotated for 60 s at 3500 rpm. In Fig. 11b, only a fraction of the 15 μm particles sedimentated at the end of the separation chamber, and almost no 8 μm particles sedimentated. The recovery ratio is only 40%. The results show that the chip can remove small particles but is less than optimal for capturing 15 μm particles.

According to the theoretical analysis, reducing the flow rate without changing the rotation speed should allow smaller particles to be captured. In this study, we reduce the structure depth of the chip to 70 μm to reduce the flow rate. The simulation results show that the chip can sort 15 μm from 8 μm particles (see Fig. 12a). Experiments were carried out with the mixture described above of 15 and 8 μm particles, and the results are shown in Fig. 12b. Almost all 15 μm particles sedimentate in the separation chamber and the 8 μm particles are almost all removed. The recovery ratio is 95.2% ± 3.4%, and the separation purity is 80.0% ± 2.6%.

Fig. 12c shows that 15 μm particles sedimentate in traps 2–6, which is a wider trap range than that of the 25 μm particles. This is consistent with the simulation analysis (see the ESI†), which indicates that the smaller particles are distributed more broadly at the inlet of the separation chamber, resulting in the larger range of sedimentation in the capture trap. However, this phenomenon does not affect the capability of the chip to capture particles, so it is possible to sort small particles with small size differences by reducing the flow rate while maintaining the rotation speed.

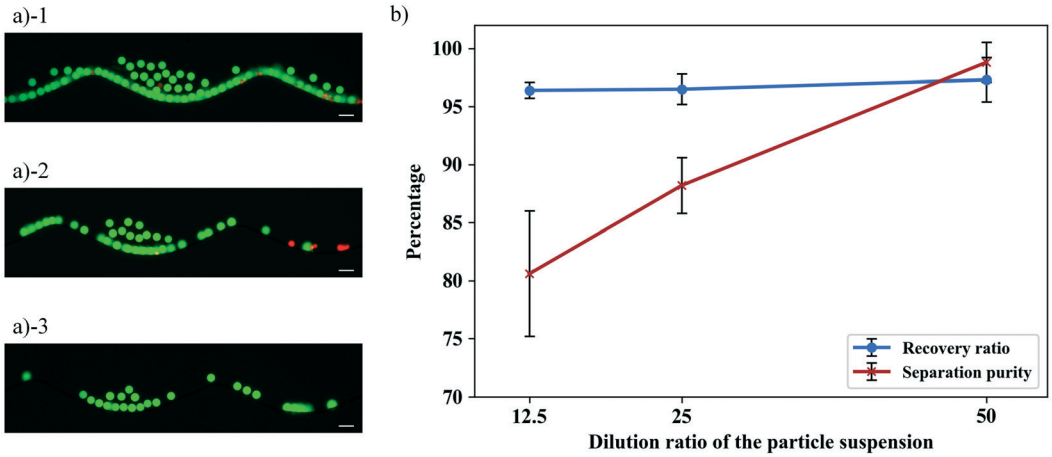

Fig. 9 Composite images of fluorescent green 25 μm particles and fluorescent red 12 μm particles at the bottom of the capture trap of the separation chamber in the dark field. Panels a-1–a-3 show the experimental results for a particle suspension mixed in equal volume and then diluted 12.5 times, 25 times, and 50 times, respectively (scale bars: 50 μm). Panel b shows the recovery ratio and separation purity of the particle suspension as a function of particle concentration (n = 3).

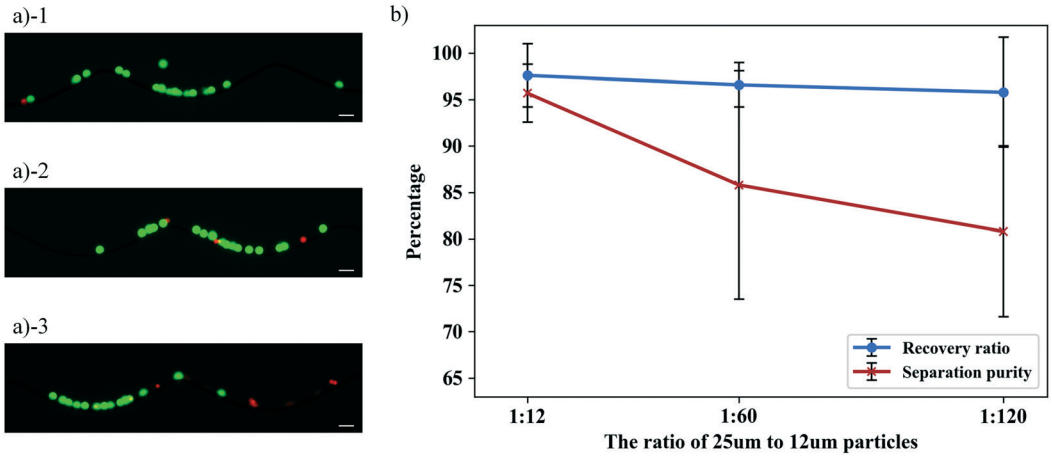

Fig. 10 Composite images of large fluorescent green particles and small fluorescent red particles at the bottom of capture trap of the separation chamber in the dark field. Panels a-1–a-3 show the experimental results of samples with large-to-small particle ratios of 1:12, 1:60, and 1:120, respectively (scale bars: 50 μm). Panel b shows the recovery ratio and separation purity of the particle suspension as a function of the particle ratio (n = 3).

4.7 Analysis of cell-sorting performance

The separation of circulating tumour cells from WBCs is a challenge in circulating tumour cell enrichment.[24] Therefore, we used the proposed centrifugal cell-sorting chip with a flow rectifier to sort rare tumour cells from WBCs. First, the red blood cells in whole blood were lysed, and then the WBCs were resuspended in phosphate buffered saline to obtain a suspension with a high concentration of up to 2.5×10^6 mL^{-1}. Next, the WBC suspension obtained was mixed in equal volume with LNCaP cells at a concentration of 1×10^5 mL^{-1}, and the mixture was introduced into the chip.

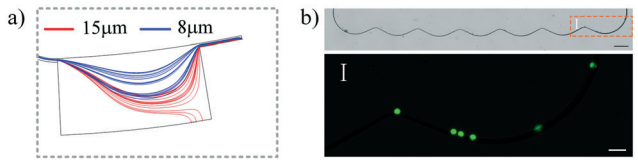

Fig. 11 Panel a) shows the numerical simulation of the particle trajectory in the separation chamber. Panel b) shows the distribution of particles in the separation chamber (scale bars: 200 μm). The lower panel (I) shows the composite images of fluorescent green 15 μm particles and fluorescent red 8 μm particles at the bottom of the capture trap of the separation chamber in the dark field (scale bars: 50 μm).

Fig. 13a shows the cell sedimentation positions and fluorescence images of tumour cells in the separation chamber. Tumour cells with diameters varying from 19.03 to 26.98 μm are captured, whereas only a few WBCs are trapped in the capture traps. This result shows that the chip offers excellent cell-sorting performance.

The sedimentation of several WBCs in the separation chamber is possibly due to the interaction between cells at high concentrations,[25] which affects the WBC trajectories.

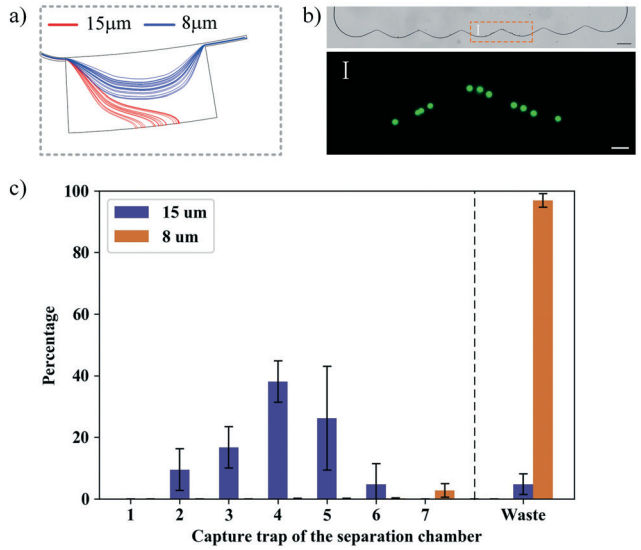

Fig. 12 Panel a) shows the numerical simulation of the particle trajectory in the separation chamber. Panel b) shows the distribution of particles in the separation chamber (scale bars: 200 μm). Lower panel (I) shows the composite images of fluorescent green 15 μm particles and fluorescent red 12 μm particles at the bottom of the capture trap of the separation chamber in the dark field (scale bars: 50 μm). Panel c) shows the percent of each type of particle in the various traps of the separation chamber (n = 3).

Fig. 13b shows the cell sedimentation in the waste chamber. Several tumour cells with diameters varying from 18.99 to 21.15 μm flow out of the separation chamber, resulting in a loss of tumour cells. The smaller tumour cells that flow out of the separation chamber with a non-negligible probability may have reached the sorting limit of the chip. We counted tumour cells and WBCs according to their morphology and fluorescence labelling. The recovery ratio of tumour cells is 90.4% ± 2.4%, and the separation purity is 83.0% ± 3.8%. Fig. 13c shows that almost all WBCs (diameters from 7.39 to 14.69 μm) are in the waste chamber. The WBC removal ratio is 99.3% ± 0.1%.

Fig. 14 shows the distribution of tumour cells and WBCs in each capture trap compared with that in the waste chamber for the rotation speed of 3500 rpm. Most tumour cells are captured in the separation chamber, whereas almost all WBCs are removed. The tumour cells are mainly in capture traps 3–7, which differs from the sedimentation position of the particles. The more dispersed sedimentation of tumour cells compared with the particles is attributed to the vertical dispersion of cells at the separation-chamber inlet, which in turn is caused by the broad range of tumour cell diameters (19.03 to 26.98 μm). In addition, the sedimentation position of the cells is farther in the separation chamber relative to the particles, possibly because of the cell deformation. Deformation of a particle causes nonlinear lateral migration, which is caused by the requirement that velocity matches stress at the particle interface. The deformation-induced lift force increases with particle deformation, with the direction of migration being predominantly toward the centreline of the channel.[26]

In the channel, deformable particles are positioned higher than rigid particles due to the superposition of the deformation-induced lift force and the inertial lift force, as shown in Fig. S5.† However, the higher the particles are positioned at the inlet, the farther they sedimentate in the separation chamber. Therefore, the sedimentation position of the deformable cells is farther in the separation chamber than the rigid particles, so that some cells reach the chip capture limit and flow out of the separation chamber, reducing the recovery ratio. In general, these cell-sorting results show that the proposed chip can separate deformable biological particles by size.

5 Conclusions

This paper presents a cell-sorting centrifugal microfluidic chip with a flow rectifier. First, the numerical simulation results for the outlet flow rate of the sample chamber show that the use of a flow rectifier promotes the steady outlet flow rate. This conclusion is verified by particle experiments that show that the fluid in the channel indeed undergoes steady flow. This centrifugal microfluidic chip thus alleviates the problems caused by particle sedimentation in the sample chamber and non-steady flow during centrifugation. As a result, the recovery ratio increases by 27.5%, and the purity increases by 63.2%.

Particle trajectories are also simulated at different rotation speeds, and the results reflect the effectiveness of the chip. At a rotation speed of 4000 rpm, a vortex develops in the separation chamber and affects the particle trajectories, thereby reducing the separation purity. The results of the particle experiments show that the chip offers excellent sorting performance at rotation speeds of 2500–3500 rpm. At 4000 rpm, the particle-separation purity decreases because of the vortex, which is consistent with the simulation results.

Moreover, experimental results of particle suspensions of varying concentrations and ratios show that the separation purity increases to nearly 100% with decreasing particle-suspension concentration and ratio, whereas the recovery ratio remains unchanged. To further analyse the chip sorting performance, we experimented with mixtures of 15 and 8 μm particles (ratio 1 : 200). With the chip depth set to 70 μm, the recovery ratio and separation purity are 95.2% ± 3.4% and 80.0% ± 2.6%, respectively. Finally, the proposed chip is used to sort tumour cells from WBCs (ratio 1 : 25). The recovery ratio of tumour cells is 90.4% ± 2.4%, and the separation purity is 83.0% ± 3.8%.

In this study, the volume of the sample is 1 μL, and 3 μL volume of sample can be operated by the chip with 3 parallel microstructures. The sample volume is small for most practical applications. However, this method can increase the sample-chamber volume by expanding the sample-chamber area. Besides, the sample volume that the chip operates can be expanded by increasing the number of parallel

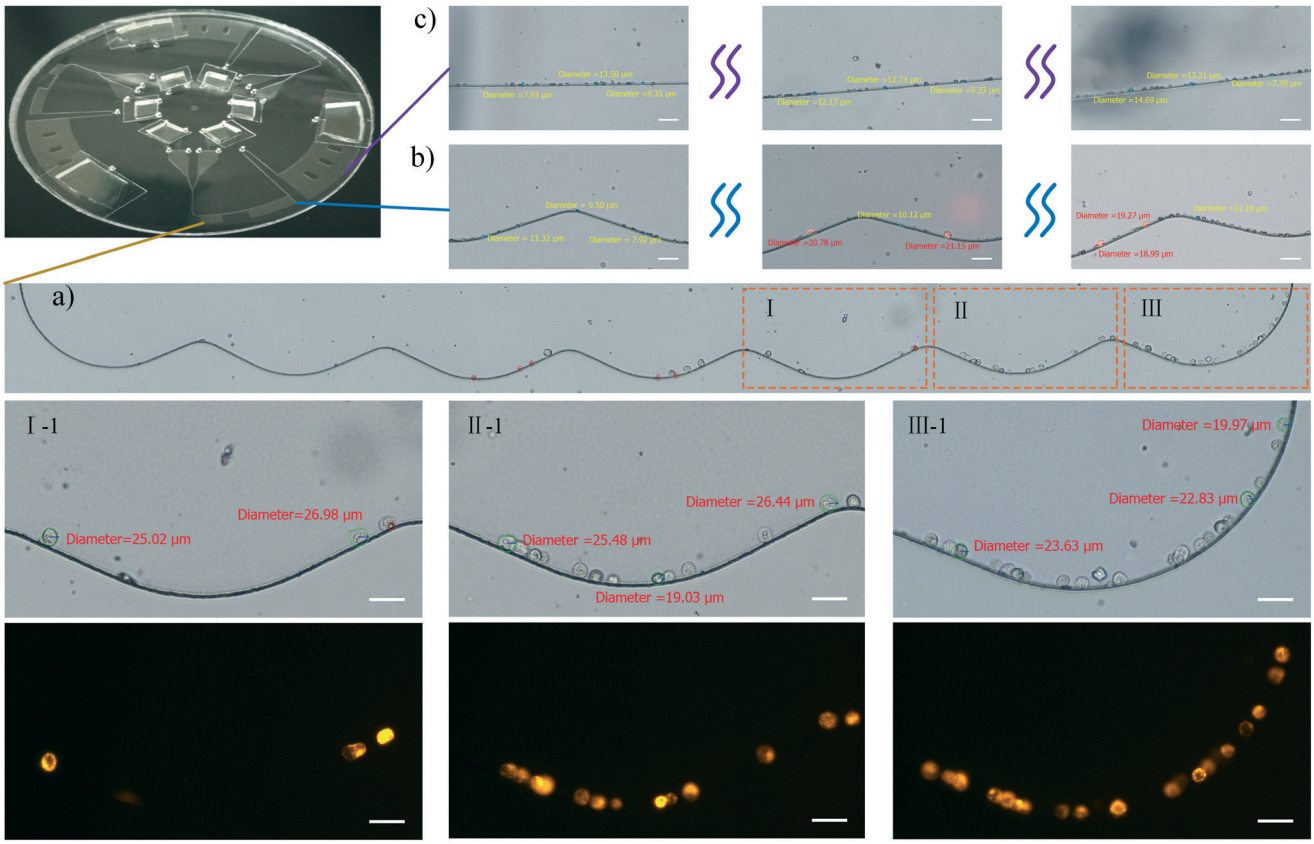

Fig. 13 Images of prostate-cancer cells and WBCs in bright and dark fields with prostate cancer cells in yellow in the dark field and WBCs marked with red circles in the bright field (scale bars: 50 μm). Panel a) shows the cell sedimentation in the separation chamber. Panels I-1–III-1 show enlarged views of areas I–III, respectively, and indicate the range of tumour cell diameters. Panels b) and c) show the sedimentation of cells in the waste chamber, which shows that almost all WBCs terminate in the waste chamber, whereas only a few tumour cells escape the separation chamber.

microstructures on the chip. Therefore, this method has a large expansion space to meet more practical application requirements.

In conclusion, the proposed chip thus offers stable sorting results, which makes it promising for the purification of rare cells and for extensive use in biomedical research.

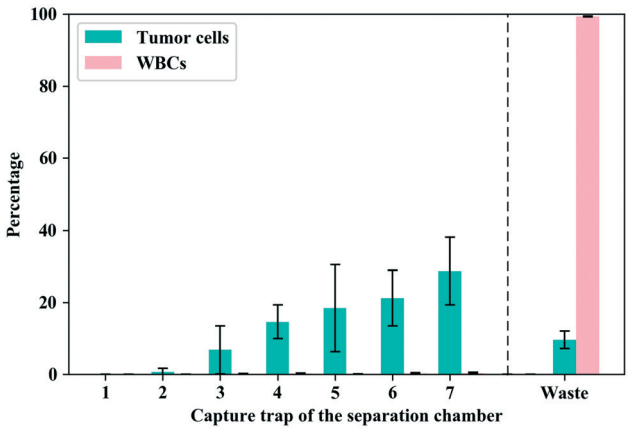

Fig. 14 Fraction of tumour cells and WBCs in capture traps compared with that in the waste chamber. Rotation speed is 3500 rpm (n = 3).

Author contributions

J. Y. M.: designed the study, carried out theoretical analysis, fabricated the devices, prepared the samples, carried out the experiments, evaluated the data and wrote the paper. Y. H. W.: proposed the concept of the work, carried out theoretical analysis, supervised and provided funding for the study. Y. S. L.: proposed the concept of the work, carried out theoretical analysis, and supervised the study. Y. J.: contributed to parts of the modeling and simulation. M. Y.: cultured the cancer cells, prepared the cell samples, and described the preparation of cell samples. H. Q. Z.: provided the cancer cells and white blood cells.

Conflicts of interest

There are no conflicts to declare.

Acknowledgements

This work was supported by the National Natural Science Foundation of China under Grant No. 61727813.

References

1 A. Dalili, E. Samiei and M. Hoorfar, *Analyst*, 2019, **144**, 87–113.
2 L. X. Kong, A. Perebikovsky, J. Moebius, L. Kulinsky and M. Madou, *J. Lab. Autom.*, 2016, **21**, 323–355.
3 R. Burger, D. Kirby, M. Glynn, C. Nwankire, M. O'Sullivan, J. Siegrist, D. Kinahan, G. Aguirre, G. Kijanka, R. A. Gorkin and J. Ducrée, *Curr. Opin. Chem. Biol.*, 2012, **16**, 409–414.
4 S. Haeberle, T. Brenner, R. Zengerle and J. Ducrée, *Lab Chip*, 2006, **6**, 776–781.
5 J. Zhang, Q. Guo, M. Liu and J. Yang, *J. Micromech. Microeng.*, 2008, **18**, 125025.
6 T. Li, L. Zhang, K. M. Leung and J. Yang, *J. Micromech. Microeng.*, 2010, **20**, 105024.
7 T. H. Kim, H. Hwang, R. Gorkin, M. Madou and Y. K. Cho, *Sens. Actuators, B*, 2013, **178**, 648–655.
8 D. J. Kinahan, S. M. Kearney, M. T. Glynn and J. Ducrée, *Sens. Actuators, A*, 2014, **215**, 71–76.
9 D. J. Kinahan, S. M. Kearney, N. A. Kilcawley, P. L. Early, M. T. Glynn and J. Ducrée, *PLoS One*, 2016, **11**, e0155545.
10 T. Morijiri, M. Yamada, T. Hikida and M. Seki, *Microfluid. Nanofluid.*, 2013, **14**, 1049–1057.
11 S. T. Moen, C. L. Hatcher and A. K. Singh, *PLoS One*, 2016, **11**, e0153137.
12 Y. Sun and P. Sethu, *Bioengineering*, 2017, **4**, 67.
13 Y. Ukita, T. Oguro and Y. Takamura, *Biomed. Microdevices*, 2017, **19**, 24.1–24.9.
14 V. Giovanna, S. Abdelmajid, L. Malek, V. Sitruk, R. Serge, K. Schütze, C. Frédérique, F. Dominique, M. Pazzagli and V. Michel, *Am. J. Pathol.*, 2000, **156**, 57–63.
15 L. J. Wu, Y. D. Pan, X. Y. Pei, H. Chen, S. Nguyen, A. Kashyap, J. Liu and J. Wu, *Cancer Lett.*, 2012, **326**, 17–22.
16 M. Wong, *J. Thorac. Dis.*, 2012, **4**, 631.
17 T. Morijiri, S. Sunahiro, M. Senaha, M. Yamada and M. Seki, *Microfluid. Nanofluid.*, 2011, **11**, 105–110.
18 J. C. Yeo, Z. Wang and C. T. Lim, *Biomicrofluidics*, 2015, **32**, 891–904.
19 M. Madadelahi, L. F. Acosta-Soto, S. Hosseini, S. O. Martinez-Chapa and M. J. Madou, *Lab Chip*, 2020, **20**, 1318–1357.
20 Y. Zhu, Y. Chen and Y. Xu, *Sens. Actuators, B*, 2018, **276**, 313–321.
21 M. Yamada, M. Nakashima and M. Seki, *Anal. Chem.*, 2004, **76**, 5465–5471.
22 A. J. Mach, J. H. Kim, A. Arshi, S. C. Hur and D. Di Carlo, *Lab Chip*, 2011, **11**, 2827–2834.
23 K. J. Humphry, P. M. Kulkarni, D. A. Weitz, J. F. Morris and H. A. Stone, *Phys. Fluids*, 2010, **22**, 209.
24 N. Xiang, J. Wang, Q. Li, Y. Han, D. Huang and Z. Ni, *Anal. Chem.*, 2019, **91**, 10328–10334.
25 T. Tanaka, T. Ishikawa, K. Numayama-Tsuruta, Y. Imai, H. Ueno, T. Yoshimoto, N. Matsuki and T. Yamaguchi, *Biomed. Microdevices*, 2012, **14**, 25–33.
26 S. C. Hur, N. K. Henderson-Maclennan, E. R. B. Mccabe and D. Di Carlo, *Lab Chip*, 2011, **11**, 912.